

# 1 Fast dimension-reduced climate model calibration

2 Won Chang, Murali Haran, Roman Olson, and Klaus Keller

3 November 30, 2023

## 4 **Abstract**

5 What is the response of the climate system to anthropogenic forcings?  
6 This question is addressed typically using projections from climate models.  
7 The uncertainty surrounding current climate projections has important pol-  
8 icy implications. Characterizing and, if possible, reducing this uncertainty  
9 is an area of ongoing research. We consider the problem of making pro-  
10 jections of the North Atlantic meridional overturning circulation (AMOC).  
11 AMOC projections are of interest because AMOC changes may considerably  
12 impact natural and human systems. Uncertainties about climate model  
13 parameters play a key role in uncertainties in AMOC projections. When  
14 the observational data and the climate model output are high-dimensional  
15 spatial data sets, the data are typically aggregated due to computational  
16 constraints. The effects of aggregation are unclear because statistically rig-  
17 orous approaches for model parameter inference have been infeasible for  
18 high-resolution data. Here we develop a flexible and computationally effi-  
19 cient approach using principal components and basis expansions to study the  
20 effect of spatial data aggregation on parametric and projection uncertainties.  
21 Our Bayesian reduced-dimensional calibration approach allows us to study  
22 the effect of complicated error structures and data-model discrepancies on

our ability to learn about climate model parameters from high-dimensional data. Considering high-dimensional spatial observations reduces the effect of deep uncertainty associated with different priors and results in sharper projections based on our climate model. We demonstrate that our computationally efficient approach may be widely applicable to a variety of high-dimensional computer model calibration problems.

## 1 Introduction

Computer models play an important role in understanding complex physical processes in modern science and engineering. They are particularly important in climate science where climate models, complex deterministic systems used to model climate processes, are used both to study climate phenomena as well as make projections about future climate. A major source of uncertainty in climate projections is due to uncertainties about model parameters. Calibration of the parameters using observational data is hence one avenue to reduce the uncertainty in future projections. A number of issues and challenges arise when performing statistical calibration of model parameters. Because each run of the computer model is computationally expensive, computer model output is typically obtained for a relatively small sample of parameter values. Furthermore, the model output at each parameter setting may be high-dimensional and in the form of spatial fields. A sound statistical approach to this problem therefore needs to simultaneously address the spatial dependence in the data and model outputs, account for various sources of uncertainty, and remain computationally efficient.

Previous approaches for climate model calibration have relied on heavy data

aggregation, turning three-dimensional data into two or one-dimensional data (e.g. Sanso and Forest, 2009; Goes et al., 2010; Olson et al., 2012) largely due to computational considerations (cf. Schmittner et al., 2009). An important and interesting question is what information, if any, is lost by this data aggregation. This is a largely unanswered question due to the inability of existing methods to analyze large spatial data sets of both computer model output and observations. Throughout this manuscript we will use “large” to refer to data sets that comprise over tens of thousands of spatial observations. Here we develop a computationally efficient approach that handles large data sets. This approach gives us the freedom to carry out a careful study of the effects of data aggregation, for example comparing calibration based on unaggregated three-dimensional data with calibration based on aggregated two-dimensional data. Our approach also enables to investigate the interaction between data aggregation and data-model discrepancies and errors when inferring computer model parameters. Our study addresses the questions of (i) whether aggregation is harmful or helpful, and (ii) how observations may be collected and processed in order to calibrate climate models and make projections with them.

We adopted a Gaussian process based approach to the calibration problem (Sacks et al., 1989; Kennedy and O’Hagan, 2001). Gaussian processes provide flexible statistical interpolators or “emulators” of the computer model across various parameter settings and are therefore attractive for climate model calibration (cf. Sanso and Forest, 2009; Bhat et al., 2012). Unfortunately, the likelihood evaluations involved in fitting such models can become prohibitive with high-dimensional spatial data due to the expensive matrix operations involved. Current approaches for high-dimensional computer model calibration can reduce the computational

71 burden and make likelihood evaluation feasible for moderately large datasets (spa-  
72 tial fields observed at a few thousand locations) or datasets that are on a regular  
73 and complete grid (Higdon et al., 2008; Bhat et al., 2012; Bayarri et al., 2007).  
74 However, to the best of our knowledge, no current calibration approach can over-  
75 come the computational challenge of dealing with large spatial data sets on a  
76 highly irregular grid.

77 The scientific problem motivating the statistical analysis is to project the future  
78 state of the North Atlantic meridional overturning circulation (AMOC) in response  
79 to anthropogenic climate forcing. The AMOC is a large-scale ocean circulation  
80 that transports cold and dense water equatorward in deep North Atlantic, and  
81 warm and salty water poleward in the upper layers of North Atlantic. The AMOC  
82 might show a persistent weakening in response to anthropogenic forcing. Because  
83 the AMOC plays an important role in heat and carbon transport, an AMOC  
84 weakening is projected to have considerable impacts on climate, and, in response,  
85 on natural and human systems (cf. Alley et al., 2007; Keller et al., 2005, 2007).  
86 We use previously published ensemble runs of the University of Victoria Earth  
87 System Climate Model (UVic ESCM) (Weaver et al., 2001) to set up an example  
88 calibration problem. Vertical ocean mixing is important in projecting the AMOC  
89 (Wunsch and Ferrari, 2004), but much of the mixing occurs on scales below that  
90 of the UVic ESCM, hence mixing is “parameterized” (cf. Weaver et al., 2001;  
91 Schmittner et al., 2009; Goes et al., 2010) using a “vertical background diffusivity”  
92 ( $K_{bg}$ ). The AMOC projections depend on the  $K_{bg}$  parameter values (e.g. Goes  
93 et al., 2010). The value of  $K_{bg}$  is uncertain; it therefore needs to be calibrated  
94 using observations of the climate that are informative about  $K_{bg}$  (cf. Goes et al.,  
95 2010; Bhat et al., 2012).

Here, we calibrate  $K_{bg}$  using observations of ocean potential temperature from World Ocean Atlas 2009 (Antonov et al., 2010; Locarnini et al., 2010).  $K_{bg}$  affects the depth of the oceanic pycnocline (Gnanadesikan, 1999) and the AMOC (Bryan, 1987; Goes et al., 2010). As a consequence, models with different  $K_{bg}$  values are expected to result in different ocean temperature distributions. Ocean temperatures are therefore informative about  $K_{bg}$ . We provide a detailed description of the data in Section 4. Note that both the UVic ESCM output and the observational data are spatial data sets with more than 60,000 spatial locations. Of particular interest is how data aggregation affects the calibration result for  $K_{bg}$ . Often observations of climate and climate model outputs are 3-D spatial fields. When the spatial data sets are large it is common practice to aggregate them into 1-D or 2-D patterns (i.e. Sanso and Forest, 2009; Drignei et al., 2008; Forest et al., 2008; Goes et al., 2010; Bhat et al., 2012) either to avoid computational issues or because the skill of the models at higher resolution may not always be trusted.

We describe a new approach that enables calibration with large spatial data sets without doing data aggregation. While our methodology has been developed in the context of high-dimensional spatial fields, it applies more generally. In our simulated examples, we have shown that the method can handle complicated model-observation discrepancy processes without sacrificing computational efficiency. Our study suggests that data aggregation can cause considerable information loss. Reducing the data aggregation can enable valuable new insights and considerably reduce parametric and projection uncertainty.

The remainder of this paper is organized as follows. In Section 2 we describe our two-stage framework for climate model calibration and the associated computational challenges. In Section 3 we propose a general model calibration approach

in a reduced dimensional space that uses a combination of principal components and a basis representation to overcome the computational challenges. In Section 4 we describe the data and provide implementation details and in Section 5 we discuss the results from simulated examples and real data. We conclude this paper with caveats and future directions in Section 6.

## 2 Model Calibration Framework

Our computer model calibration framework consists of two stages, (i) model emulation and (ii) parameter calibration (Bayarri et al., 2007; Bhat et al., 2012). First, we construct an emulator that interpolates computer model outputs at different parameter settings using Gaussian random fields (Sacks et al., 1989). This can be viewed as statistical interpolation or “kriging” (Cressie, 1994) in the computer model parameter space. Second, we infer the computer model parameters by relating observational data to computer model output using the emulator, while considering observational error and allowing for systematic discrepancies between the model and observations (Kennedy and O’Hagan, 2001). Note that this two-stage approach has some advantages over fully Bayesian methods that combine the two stages into a single inferential step. By ‘cutting feedback’ or modularization (Rougier, 2008; Bhat et al., 2012; Liu et al., 2009), this two-stage approach ensures that inference in the emulation stage is not contaminated by model discrepancy and observational error. In addition, separating the emulation stage from calibration provides an easier way to diagnose the accuracy of an emulator. Furthermore, computations are faster and parameter identifiability problems are reduced.

Let  $Y(\mathbf{s}, \boldsymbol{\theta})$  denote the computer model output at the spatial location  $\mathbf{s} =$

144 (longitude, latitude, depth)  $\in \mathcal{S} \subseteq \mathbb{R}^3$  and the model parameter setting  $\boldsymbol{\theta} \in \boldsymbol{\Theta} \subseteq$   
 145  $\mathbb{R}^3$ , where  $\mathcal{S}$  is the spatial domain of the process and  $\boldsymbol{\Theta}$  is the computer model  
 146 parameter space.  $Z(\mathbf{s})$  is the corresponding observation at the spatial location  $\mathbf{s}$ .  
 147 Since each run of the climate model is computationally expensive, we can obtain  
 148 computer model outputs only for a relatively small number of design points  $p$ .  
 149 We denote these design points in the parameter space by  $\boldsymbol{\theta}_1, \dots, \boldsymbol{\theta}_p \in \mathcal{D} \subseteq \mathbb{R}^3$ .  
 150 Let  $\mathbf{Y}_i \in \mathbb{R}^n$  be the computer model output at each parameter setting  $\boldsymbol{\theta}_i$  for  
 151  $i = 1, \dots, p$ . Each computer model output  $\mathbf{Y}_i = (Y(\mathbf{s}_1, \boldsymbol{\theta}_i), \dots, Y(\mathbf{s}_n, \boldsymbol{\theta}_i))^T$  is a  
 152 spatial process observed at  $n$  different spatial locations  $(\mathbf{s}_1, \dots, \mathbf{s}_n)$ . Let  $\mathbf{Y}$  be the  
 153 vector of concatenated computer model outputs such that  $\mathbf{Y} = (\mathbf{Y}_1, \dots, \mathbf{Y}_p)^T$ . We  
 154 also denote the observed spatial process at  $n$  locations by  $\mathbf{Z} = (Z(\mathbf{s}_1), \dots, Z(\mathbf{s}_n))^T$ .  
 155 Note that we assume that the locations for each model output and observation data  
 156 are the same. If they are different, one can interpolate either of them depending  
 157 on which one has a higher resolution. Our objective is to infer the parameter  $\boldsymbol{\theta}$  by  
 158 combining information from  $\mathbf{Z}$  and  $\mathbf{Y}$ .

## 159 2.1 Two-Stage Emulation and Calibration

160 We first outline our general framework for emulation and calibration.

### 161 Model Emulation Using Gaussian Random Fields

Following Bhat et al. (2012) we approximate the climate model using a Gaussian process such that

$$\mathbf{Y} \sim N(\mu_{\boldsymbol{\beta}}, \Sigma(\boldsymbol{\xi}_y)),$$

162 where  $\mu_{\beta}$  is a linear mean function  $\mathbf{X}\beta$  with a  $np \times b$  covariate matrix  $\mathbf{X}$  and a  
 163 vector of regression coefficient  $\beta$ . The covariates in  $\mathbf{X}$  are the spatial locations  
 164 (e.g. latitude, longitude, and depth) and the climate parameters. The covariate  
 165 matrix  $\mathbf{X}$  contains all the spatial coordinates and the parameter settings used to  
 166 define the covariance matrix  $\Sigma(\xi_y)$ .  $\xi_y$  is a vector of parameters determining the  
 167 covariance matrix  $\Sigma(\xi_y)$ . We fit a Gaussian random field to  $\mathbf{Y}$  by finding the  
 168 maximum likelihood estimate (MLE) of  $(\beta, \xi_y)$ , denoted by  $(\hat{\beta}, \hat{\xi}_y)$ .

169 The fitted Gaussian random field defines the probability model for the com-  
 170 puter model output at any location  $\mathbf{s} \in \mathcal{S}$  and parameter setting  $\theta \in \Theta$ . Therefore,  
 171 the Gaussian process model provides a predictive distribution of computer model  
 172 output at any untried value of  $\theta$  given the existing output  $\mathbf{Y}$  (Sacks et al., 1989).  
 173 We denote the resulting interpolation process by  $\eta(\theta, \mathbf{Y})$  and call it an emula-  
 174 tor. This emulator acts as an interpolator while at the same time providing a  
 175 quantification of interpolation uncertainty.

## 176 Model Calibration Using Gaussian Random Field Model

177 Once an emulator  $\eta(\theta, \mathbf{Y})$  is available, we model the observational data  $\mathbf{Z}$ ,

$$\mathbf{Z} = \eta(\mathbf{Y}, \theta) + \delta + \epsilon, \quad (1)$$

178 where  $\epsilon \sim N(\mathbf{0}, \sigma^2 \mathbf{I})$  is independently and identically distributed observational  
 179 error and  $\delta$  is a data-model discrepancy term.  $\delta$  is also modeled as a Gaussian  
 180 process, thus  $\delta \sim N(\mathbf{0}, \Sigma_d(\xi_d))$  with a spatial covariance matrix  $\Sigma_d(\xi_d)$  between  
 181 the locations  $\mathbf{s}_1, \dots, \mathbf{s}_n$  and a vector of covariance parameters  $\xi_d$ . The details re-  
 182 garding the specification of the covariance function are provided in Section 3.2.2.



183 This discrepancy term is crucial for parameter calibration (cf. Bayarri et al., 2007;  
 184 Bhat et al., 2010). Note that this problem is ill-posed without any prior informa-  
 185 tion for  $\xi_d$ , so an informative prior is necessary. Our inference for  $\theta$ ,  $\xi_d$  and  $\sigma^2$  is  
 186 based on their resulting posterior distribution.

## 187 **2.2 Challenges with High-Dimensional Data**

188 High-dimensional datasets pose considerable computational challenges due to the  
 189 expensive likelihood function calculations that involve high-dimensional matrix  
 190 computations. This is an important issue because model output and observational  
 191 data in many fields, particularly climate science, tend to be high-dimensional. For  
 192 instance, in the calibration problem described in Section 4, the dimensionality  
 193 of the model output and the observational data is  $n = 984$  in the 2-D case and  
 194  $n = 61,051$  in the 3-D case. The latter example involves prohibitive computations  
 195 with naïve implementations (discussed and explained below). For instance, with  $n$ -  
 196 dimensional climate model outputs at  $p$  different parameter settings, evaluation of  
 197 the likelihood function requires  $\mathcal{O}(n^3 p^3)$  operations. Therefore numerical methods  
 198 such as Newton-Raphson or MCMC algorithms become infeasible. For the 3-D  
 199 case, this translates to  $7.585 \times 10^{13}$  flops of computations, which takes more than  
 200 3 hours for a high performance modern single-core processor.

## 3 Model Calibration with High-Dimensional Spatial Data

We develop a dimension reduction approach based on spatial basis functions to increase computational efficiency. Spatial basis functions can map high-dimensional data into a low-dimensional space (Bayarri et al., 2007) and find a representation of the probability model that results in a lower computational cost for likelihood evaluations (Higdon et al., 2008; Bhat et al., 2012). Since there may be a trade-off between parsimony and accurate inference, it is crucial to find a set of spatial basis functions that gives a computationally feasible likelihood formulation without a considerable loss of information. Below, we review drawbacks to the current approaches in the context of high-dimensional spatial data and propose a new approach to overcome these limitations.

### 3.1 Current Approaches

A few different approaches to climate model calibration with multivariate computer model outputs have been developed in recent years, including Bayarri et al. (2007), Higdon et al. (2008), and Bhat et al. (2012). These approaches, however, are not readily applicable to the 3D model output and observations we consider here due to the following reasons. First, in spite of the gains in computational efficiency likelihood evaluations remain computationally prohibitive. The computational cost of a single likelihood evaluation in the emulation step in Bhat et al. (2012) scales as  $\mathcal{O}(nJ^2)$  where  $J$  is the dimensionality of the basis matrix. In Higdon et al. (2008), the computational cost scales with  $\mathcal{O}(p^3 J_y^3)$  where  $J_y$  is the

223 number of principal components used to represent the data. For the 3D calibra-  
 224 tion problem we consider,  $n$  is 61,051,  $J$  is around 20,000 and  $J_y$  is around 20.  
 225 Second, the transformation based on the basis matrix may not be applicable to  
 226 two or three-dimensional spatial data. Using a wavelet transformation (Bayarri  
 227 et al., 2007) requires the same dyadic (a power of 2) number of data points for  
 228 each spatial dimension, and the data need to be on a regular grid without missing  
 229 values; irregular data and missing values are common in climate model calibration  
 230 problems. In addition, conducting Bayesian inference on the joint posterior dis-  
 231 tribution may pose difficulties, both computationally as well as in terms of prior  
 232 specification and identifiability issues. For example, Higdon et al. (2008) requires  
 233 estimating  $4 \times J_y + 1$  parameters, which translates to an 81-dimensional distribution  
 234 for the 3-D case in Section 4.

## 235 **3.2 Reduced Dimensional Model Calibration**

236 Our method to overcome the aforementioned challenges relies on (i) represent-  
 237 ing the spatial field using principal components, and (ii) emulating each principal  
 238 component separately. Instead of using principal component basis to reduce the  
 239 complexity of matrix computation as in Higdon et al. (2008), we use it to map  
 240 the computer model outputs into a low-dimensional space and construct an em-  
 241 ulator in that space directly. Since the principal components are uncorrelated by  
 242 construction, we can build the emulator by constructing a 1-dimensional Gaus-  
 243 sian process for each principal component in parallel. Fitting Gaussian random  
 244 fields for each principal component requires estimation of only 5 parameters. The  
 245 likelihood evaluations involve covariance matrices of size  $p \times p$ . These features

allow us to construct the emulator in a computationally efficient and highly automated manner. Moreover, since the principal component transformation can be applied to non-dyadic spatial data with irregular locations, it has a broader range of application than wavelet transformations. In the calibration step, we develop an approach to map the observational data into a low dimensional space.

### 3.2.1 Computer Model Emulation

The first step of this approach is to find the basis matrix for computer model output. We consider the computer model outputs as an  $n$ -dimensional dataset with  $p$  replications and find the principal component basis. Let  $\mathbf{M}$  denote the  $p \times n$  matrix storing the computer model outputs  $\mathbf{Y}_1, \dots, \mathbf{Y}_p$  such that

$$\mathbf{M} = \begin{pmatrix} \mathbf{Y}_1^T \\ \vdots \\ \mathbf{Y}_p^T \end{pmatrix}. \quad (2)$$

Following the standard process of finding principal components, we first preprocess the computer model outputs to make the column means of the matrix  $\mathbf{M}$  all 0's. Applying singular value decomposition, we find the scaled eigenvectors  $\mathbf{k}_1 = \sqrt{\lambda_1} \mathbf{e}_1, \dots, \mathbf{k}_p = \sqrt{\lambda_p} \mathbf{e}_p$  where  $\lambda_1 > \lambda_2 > \dots > \lambda_p$  are the ordered eigenvalues and  $\mathbf{e}_1, \dots, \mathbf{e}_p$  are the corresponding eigenvectors of the covariance matrix of  $\mathbf{M}$ , where  $J_y \ll p$  is the number of principal components that we decide to use in the emulator. One can choose the number of principal components by looking at the proportion of explained variation given by  $\frac{\sum_{i=1}^{J_y} \lambda_i}{\sum_{i=1}^p \lambda_i}$ . We define the basis matrix for computer model output by  $\mathbf{K}_y = (\mathbf{k}_1, \dots, \mathbf{k}_{J_y})$ .

For each parameter setting  $\boldsymbol{\theta}_i$  ( $i = 1, \dots, p$ ), the first  $J_y$  principal components  $\mathbf{Y}_i^R = (Y_{i1}^R, \dots, Y_{iJ_y}^R)^T$  are computed by

$$\mathbf{Y}_i^R = (\mathbf{K}_y^T \mathbf{K}_y)^{-1} \mathbf{K}_y^T \mathbf{Y}_i.$$

Let  $\mathbf{Y}^R = (\mathbf{Y}_1^R, \dots, \mathbf{Y}_p^R)^T$ , hence each element of this matrix  $\{\mathbf{Y}^R\}_{ij} = Y_{ij}^R$  is the  $j$ th principal component at the  $i$ th computer model parameter setting. Since the columns in  $\mathbf{K}_y$  are orthogonal, the principal components found here are uncorrelated to each other and this leads us to a parallelized emulator construction that is similar to the wavelet transformation approach in Bayarri et al. (2007). For each  $j$ th principal component across the parameter settings (i.e. for each  $j$ th column of  $\mathbf{Y}^R$ ), we construct a Gaussian random field with the squared exponential covariance function such that

$$\text{Cov}(Y_{kj}^R, Y_{lj}^R) = \kappa_{y,j} \exp \left( - \sum_{i=1}^3 \frac{|\theta_{ik} - \theta_{il}|^2}{\phi_{y,ij}^2} \right) + \zeta_{y,j} 1(k = l) \quad (3)$$

with partial sill  $\kappa_{y,j}$ , nugget  $\zeta_{y,j}$ , and range parameters  $\boldsymbol{\phi}_{y,j} = (\phi_{y,1j}, \phi_{y,2j}, \phi_{y,3j})^T$ . Leave-10-percent-out cross-validation experiments with 50 different randomly generated scenarios indicate that the squared exponential covariance shows a better fit than other alternatives such as exponential covariance.

We denote the collection of emulator parameters for each  $j$ th principal component by  $\boldsymbol{\xi}_{y,j} = (\kappa_{y,j}, \zeta_{y,j}, \boldsymbol{\phi}_{y,j})^T$ . One can construct the emulator by finding the MLE  $\hat{\boldsymbol{\xi}}_{y,j}$  for each  $j$  separately. The emulator  $\boldsymbol{\eta}(\boldsymbol{\theta}, \mathbf{Y}^R)$  is the collection of predictive processes of  $J_y$  principal components at  $\boldsymbol{\theta}$  defined by the covariance function (3) and the MLEs  $\hat{\boldsymbol{\xi}}_{y,1}, \dots, \hat{\boldsymbol{\xi}}_{y,J_y}$ . Note that even though we constructed the em-

ulator in terms of the principal components, we can make a projection  $\mathbf{Y}^*$  in the original space at a new parameter setting  $\boldsymbol{\theta}^*$  by computing

$$\mathbf{Y}^* = \mathbf{K}_y \boldsymbol{\eta}(\boldsymbol{\theta}^*, \mathbf{Y}^R).$$

277 To summarize, the emulation step uses the data  $\mathbf{Y}_1^R, \dots, \mathbf{Y}_{J_y}^R$  of dimension  $p$  and  
 278 compute MLEs  $\hat{\boldsymbol{\xi}}_1, \dots, \hat{\boldsymbol{\xi}}_{J_y}$ . Hence, the computational cost is reduced from  $\mathcal{O}(n^3 p^3)$   
 279 to  $\mathcal{O}(J_y p^3)$  when compared to a naïve approach. The resulting fitted model is then  
 280 used for the calibration step as described in the following section.

### 281 3.2.2 Computer Model Calibration

Using  $\boldsymbol{\eta}(\boldsymbol{\theta}, \mathbf{Y}^R)$ , the emulator for the principal components, we define the model for observational data by

$$\mathbf{Z} = \mathbf{K}_y \boldsymbol{\eta}(\boldsymbol{\theta}, \mathbf{Y}^R) + \mathbf{K}_d \boldsymbol{\nu} + \boldsymbol{\epsilon},$$

282 where  $\mathbf{K}_d \boldsymbol{\nu}$  is a kernel convolution representation (Higdon, 1998) of the discrepancy  
 283  $\boldsymbol{\delta}$ .  $\boldsymbol{\nu}$  is a vector of independent and identical Normal random variates at  $J_d \ll n$   
 284 locations,  $\boldsymbol{\nu} \sim N(\mathbf{0}, \mathbf{I}_{J_d})$ .  $\mathbf{a}_1, \dots, \mathbf{a}_{J_d} \in \mathcal{S}$ . We define the kernel basis by

$$(\mathbf{K}_d)_{ij} = \sqrt{\kappa_d} \exp \left( -\frac{g(s_{1i}, s_{2i}, a_{1j}, a_{2j})}{\phi_{d,1}} - \frac{|s_{3i} - a_{3j}|}{\phi_{d,2}} \right), \quad (4)$$

where  $s_{ki}$  and  $a_{kj}$  are the  $k$ th elements of  $\mathbf{s}_i$  and  $\mathbf{a}_j$  respectively.  $\kappa_d$  is the precision parameter determining the magnitude of discrepancy, and  $\phi_{d,1}, \phi_{d,2} > 0$  are the range parameters specifying the bandwidth of kernels. The geodesic distance function measures the great circle distance between two points on the Earth's surface.

The function  $g(s_{1i}, s_{2i}, a_{1j}, a_{2j})$  is given by

$$r \arccos(\sin(s_{2i}) \sin(a_{2j}) + \cos(\sin(s_{2i}) \cos(a_{2j}) \cos |s_{1i} - a_{1j}|),$$

where  $r$  is the radius of Earth (6378.388km). By following Higdon et al. (2008), the range parameters are pre-specified by scientific expert judgment; this reduces computations and identifiability issues. The kernel function in (4) yields a valid covariance under geodesic distance since it is strictly positive definite on a sphere (Gneiting, 2011). We assumed separability for distance along the surface and distance along the depth. The resulting process is approximately twice differentiable (Zhu and Wu, 2010), which produces a reasonable model for discrepancy. Even though the discrepancy model implies an isotropic discrepancy process (Higdon, 2002), the resulting process is flexible enough to capture the general trend in the discrepancy.

Instead of using the model (4) directly, we conduct calibration with reduced-dimensional data for computational efficiency. Let  $\mathbf{Z}^R$  be a reduced version of the original data such that

$$\mathbf{Z}^R = (\mathbf{K}^T \mathbf{K})^{-1} \mathbf{K}^T \mathbf{Z} = \begin{pmatrix} \boldsymbol{\eta}(\boldsymbol{\theta}, \mathbf{Y}^R) \\ \boldsymbol{\nu} \end{pmatrix} + (\mathbf{K}^T \mathbf{K})^{-1} \mathbf{K}^T \boldsymbol{\epsilon},$$

where  $\mathbf{K} = (\mathbf{K}_y \ \mathbf{K}_d)$ . The probability model of  $\mathbf{Z}^R$  is

$$\mathbf{Z}^R \sim N \left( \begin{pmatrix} \boldsymbol{\mu}_\eta \\ \mathbf{0} \end{pmatrix}, \begin{pmatrix} \Sigma_\eta & \mathbf{0} \\ \mathbf{0} & \kappa_d \mathbf{I}_{J_d} \end{pmatrix} + \sigma^2 (\mathbf{K}^T \mathbf{K})^{-1} \right), \quad (5)$$

296 where  $\boldsymbol{\mu}_\eta$  and  $\Sigma_\eta$  are the mean and covariance given by the emulator  $\boldsymbol{\eta}(\boldsymbol{\theta}, \mathbf{Y}^R)$ .  
 297 It is often helpful to apply singular value decomposition to  $\mathbf{K}_d$  and use the first  
 298  $J_d^{PC} \ll J_d$  eigenvectors  $\mathbf{K}_d^{PC}$  in place of  $\mathbf{K}_d$  to find  $\mathbf{Z}^R$ . In addition to the obvious  
 299 computational advantage, this often results in better inference since it corresponds  
 300 to a regularized estimate given by ridge regression (see Hastie et al., 2009, pg. 66);  
 301 this was corroborated by our extensive simulation studies.

302 Note that the term  $\sigma^2(\mathbf{K}^T \mathbf{K})^{-1}$  in (5) automatically adjusts the contribution  
 303 of each principal component to the calibration result. This can be illustrated by  
 304 considering the model without the discrepancy, and the variance in the likelihood  
 305 function is simply  $\Sigma_\eta + \sigma^2(\mathbf{K}_y^T \mathbf{K}_y)^{-1}$ . Since  $(\mathbf{K}_y^T \mathbf{K}_y)^{-1}$  is a diagonal matrix and its  
 306  $i$ th diagonal element is the reciprocal of the  $i$ th eigenvalue,  $(\mathbf{K}_y^T \mathbf{K}_y)^{-1}$  inflates the  
 307 variance of principal components with small eigenvalues. Therefore, the principal  
 308 components with smaller explained variance will have less effect on the calibration  
 309 result.

310 We now briefly examine the covariance structure implied by our model. Using  
 311 the leading  $J$  principal components, the covariance between computer model out-  
 312 puts at two different spatial and parametric coordinates  $(\mathbf{s}_1, \boldsymbol{\theta}_1)$  and  $(\mathbf{s}_2, \boldsymbol{\theta}_2)$  can  
 313 be written as

$$\begin{aligned}
 \text{Cov}(Y(\mathbf{s}_1, \boldsymbol{\theta}_1), Y(\mathbf{s}_2, \boldsymbol{\theta}_2)) &\approx \text{Cov}\left(\sum_{i=1}^J \lambda_i \mathbf{e}_i(\mathbf{s}_1) w_i(\boldsymbol{\theta}_1), \sum_{j=1}^J \mathbf{e}_j(\mathbf{s}_2) w_j(\boldsymbol{\theta}_2)\right) \\
 &= \sum_{i=1}^J \sqrt{\lambda_i} \mathbf{e}_i(\mathbf{s}_1) \sqrt{\lambda_i} \mathbf{e}_i(\mathbf{s}_2) \text{Cov}(w_i(\boldsymbol{\theta}_1), w_i(\boldsymbol{\theta}_2)),
 \end{aligned}$$



where  $\mathbf{e}_i(\cdot)$  is the  $i$ th eigenfunction satisfying

$$\int \text{Cov}(Y(\theta_1, \mathbf{s}_1), Y(\theta_2, \mathbf{s}_2)) \mathbf{e}_i(\mathbf{s}_2) d\mathbf{s}_2 = \lambda_i \mathbf{e}_i(\mathbf{s}_2) \text{Cov}(w_i(\theta_1), w_i(\theta_2)),$$

with the corresponding eigenvalue  $\lambda_i$  and the process of principal component  $w_i(\cdot)$ . The leading eigenfunctions give the best approximation among all possible orthogonal bases since it minimizes the total mean square error (Jordan, 1961). Since we can assume different covariance functions for each principal component process, our model can yield a non-separable space-parameter covariance function. In contrast, if we were to assume separability such that

$$\text{Cov}(Y(\theta_1, \mathbf{s}_1), Y(\theta_2, \mathbf{s}_2)) = C_s(\mathbf{s}_1, \mathbf{s}_2) C_\theta(\theta_1, \theta_2),$$

314 for some positive definite covariance functions  $C_s$  and  $C_\theta$ , the covariance function  
315 for the  $i$ th principal component process becomes

$$\begin{aligned} \text{Cov}(w_i(\theta_1), w_i(\theta_2)) &= \text{Cov}\left(\int Y(\theta_1, \mathbf{s}_1) \mathbf{e}_i(\mathbf{s}_1) d\mathbf{s}_1, \int Y(\theta_2, \mathbf{s}_2) \mathbf{e}_i(\mathbf{s}_2) d\mathbf{s}_2\right) \\ &= \int \mathbf{e}_i(\mathbf{s}_1) \left( \int \text{Cov}(Y(\theta_1, \mathbf{s}_1), Y(\theta_2, \mathbf{s}_2)) \mathbf{e}_i(\mathbf{s}_2) d\mathbf{s}_2 \right) d\mathbf{s}_1 \\ &= C_\theta(\theta_1, \theta_2) \int \mathbf{e}_i(\mathbf{s}_1) \int \text{Cov}(\mathbf{s}_1, \mathbf{s}_2) \mathbf{e}_i(\mathbf{s}_2) d\mathbf{s}_2 d\mathbf{s}_1 \\ &= C_\theta(\theta_1, \theta_2) \lambda_i. \end{aligned}$$

316 The separability assumption therefore results in a restrictive covariance structure  
317 such that the correlation function for all principal component processes are the  
318 same. Hence even though our reduced dimensional approach utilizes a covariance  
319 that is easy to specify, it provides a richer class of covariance functions than a sepa-

320 rable covariance structure. Our cross-validation studies show that our assumption  
 321 is adequate for emulating the computer model.

## 322 Priors

323 We estimate the joint density of  $\boldsymbol{\theta}$ ,  $\kappa_d$ , and  $\sigma^2$  using the Metropolis-Hastings al-  
 324 gorithm. Following Bayarri et al. (2007), we allow for additional flexibility by  
 325 estimating the partial sill parameters  $\kappa_{y,1}, \dots, \kappa_{y,J_y}$  for the emulator. Prior spec-  
 326 ification for the parameters in the observational model is straightforward. The  
 327 discrepancy variance  $\kappa_d$  and the observational error variance  $\sigma^2$  receive inverse-  
 328 gamma priors with small shape parameter values. The prior for each parameter  
 329 being calibrated is a uniform distribution over a broad range or determined by sci-  
 330 entific knowledge. In order to stabilize the inference, we put an informative prior  
 331 to encourage  $\kappa_{y,1}, \dots, \kappa_{y,J_y}$  to vary around their estimated values in the emulation  
 332 stage.

## 333 Computing

334 The computational costs may be summarized as follows:

- 335 1. Find the basis matrix  $\mathbf{K}_y = (\sqrt{\lambda_1}\mathbf{e}_1, \dots, \sqrt{\lambda_{J_y}}\mathbf{e}_{J_y})$  by computing the singu-  
 336 lar value decomposition of  $\mathbf{M}$  in (2). This computation is of order  $\mathcal{O}(n^3)$ ,  
 337 but it needs to be done only once.
- 338 2. Compute  $\mathbf{Y}_R$  where its  $i$ th row is the transpose of  $(\mathbf{K}_y^T \mathbf{K}_y)^{-1} \mathbf{K}_y^T \mathbf{Y}_i$ .
- 339 3. Construct a Gaussian random field for each column of  $\mathbf{Y}_R$  by finding the  
 340 MLE  $\hat{\boldsymbol{\xi}}_{y,i}$  for each  $i = 1, \dots, J_y$ . The computational cost is of order  $\mathcal{O}(p^3)$   
 341 for each likelihood evaluation.

- 342 4. Compute  $\mathbf{Z}_R = (\mathbf{K}^T \mathbf{K})^{-1} \mathbf{K}^T \mathbf{Z}$ . The computational complexity of this step  
343 is  $\mathcal{O}((J_y + J_d)^3)$ .
- 344 5. Using Metropolis-Hastings, draw an MCMC sample of  $\boldsymbol{\theta}$ ,  $\sigma^2$ ,  $\kappa_d$  and  $\kappa_{y,1}, \dots, \kappa_{y,J_y}$   
345 from the joint posterior distribution based on the model in (5). The compu-  
346 tational cost for each likelihood evaluation is of order  $\mathcal{O}((J_y + J_d)^3)$ .
- 347 The overall cost of our implementation is  $\mathcal{O}(pJ_y^3)$  for the emulation step and  
348  $\mathcal{O}((J_y + J_d)^3)$  for the calibration step.

## 349 4 Implementation Details

350 Our goal is to build an emulator based on spatial output from UVic ESCM and to  
351 calibrate vertical ocean diffusivity ( $K_{bg}$ ) using ocean potential temperature data.  
352 The UVic ESCM runs are 3-dimensional patterns of the mean ocean potential  
353 temperature over 1955–2006 at  $p = 250$  parameter settings. The parameters con-  
354 trolling model outputs are vertical ocean diffusivity ( $K_{bg}$ ), anthropogenic aerosol  
355 scaling factor ( $A_{scl}$ ), and climate sensitivity ( $C_s$ ). Note that we converted long-  
356 wave radiation feedback factor, which is one of the original input parameters for  
357 UVic, into  $C_s$  using a simple spline fit. We refer to Srivier et al. for the design  
358 points and more details of this ensemble runs.

359 To avoid the problem related to model artifacts and sparse sampling, we ex-  
360 cluded data beyond 60°N and 80°S and 3000m in depth (Key et al., 2004; Schmit-  
361 tner et al., 2009; Bhat et al., 2012). UVic ESCM outputs are on a 77 (latitude)  $\times$   
362 100 (longitude)  $\times$  13 (depth) grid, but the number of locations that have non-  
363 missing observations is 65,595. The missing values occur because there is no ocean

364 at the locations in the UVic ESCM representation.

365 The observational data is on a  $180$  (latitude) $\times$   $360$  (longitude) $\times$   $33$  (depth)  
366 grid, and we remap this observed data into the Uvic model grid using a linear in-  
367 terpolation. This results in a relatively small reduction of data points to 61,051 data  
368 points. The model output locations considered in our modeling are also adjusted  
369 accordingly. We convert the observed in-situ temperature field into potential tem-  
370 perature field in order to (i) have the same measurement unit with UVic ESCM  
371 output and (ii) adjust the effect of pressure on ocean temperature. We obtain  
372 potential temperature from the in-situ temperature (Locarnini et al., 2010) and  
373 salinity fields (Antonov et al., 2010) using UNESCO equation of state (UNESCO,  
374 1981) following Bryden (1973) and Fofonoff (1977). During the conversion proce-  
375 dure, we assume a simplified ocean pressure field varying as a function of latitude  
376 and depth (Lovett, 1978). We apply our method to data at three different aggre-  
377 gation levels. In the 1-D case, we compute the vertical means at  $n = 13$  different  
378 depth points (Goes et al., 2010). In the 2-D case, the longitudinal means are  
379 computed at  $n = 984$  latitude and depth points (Bhat et al., 2012). We use the  
380 original pattern without any aggregation in the 3-D case ( $n = 61,051$ ). The num-  
381 ber of principal components is determined to have more than 90% of the explained  
382 variation. The number of components is 5 for the 1-D, 10 for the 2-D, and 20 for  
383 the 3-D case. We also tried to use 10 principal components for the 1-D, 20 for  
384 the 2-D, and 30 for the 3-D case to have more than 95% explained variation, but  
385 could not find any improvement in the calibration result.

386 We use all 250 design points in the parameter space to build the emulator.  
387 We fix  $C_s$  and  $A_{scl}$  at the default values of the UVic ESCM in the calibration  
388 stage and made an inference only for  $K_{bg}$ . The default values are 1 for  $A_{scl}$  and

389 3.81879 for  $C_s$ . One may choose to integrate out these two parameters, but since  
 390 the ocean temperature field lacks strong information about  $A_{scl}$  and  $C_s$ , their es-  
 391 timated posterior densities are overly dispersed. This introduces unnecessary bias  
 392 in the estimate of  $K_{bg}$  due to the highly non-linear relationship between climate  
 393 parameters (Olson et al., 2012), thus we decided not to integrate out those two  
 394 parameters.

395 By following Bhat et al. (2012), we assume a flat prior with a broad range for  
 396  $K_{bg}$ , from 0.05 to 0.55. The variance for the observational error ( $\sigma^2$ ) and the model  
 397 discrepancy ( $\kappa_d$ ) receive inverse-Gamma priors, and we denote them by  $\text{IG}(a_\nu, b_\nu)$   
 398 and  $\text{IG}(a_z, b_z)$ . We set the shape parameters for them by  $a_\nu = 2$  and  $a_z = 2$ . To  
 399 check the sensitivity of our approach to prior specifications, we tried four different  
 400 combinations,  $(2, 2)$ ,  $(2, 100)$ ,  $(100, 2)$ , and  $(100, 100)$  for  $b_\nu$  and  $b_s$ . The emulator  
 401 variances  $\kappa_{y,1}, \dots, \kappa_{y,J_y}$  also receive inverse-Gamma priors with a shape parameter  
 402 of 5. The scale parameters are determined to have modes at their estimated values  
 403 in the emulation stage. Because of parameter identifiability problems which in turn  
 404 affected computation, we fixed the range parameter for depth at 3000m and for  
 405 surface as 2500km. We found that a wide range of the different settings for these  
 406 parameters gave the same inference result for  $K_{bg}$  and hence our particular choices  
 407 did not affect the results. The number of knot locations for the discrepancy kernel  
 408 is 800 in the 3D case, 80 in the 2D case, and 13 in the 1D case. The number of  
 409 principal components used for the discrepancy is 200 in the 3D case, 20 in the 2D  
 410 case, and 5 in the 1D case. The number of principal components was determined  
 411 using standard practice – by ensuring that at least 95% of the variability in the  
 412 data was explained in each case. In order to check the robustness of our results, we  
 413 tried different numbers of principal components. For example, when we increased

the number of principal components to 300 in the 3D case, 30 in the 2D case and 8 in the 1D case we found that we obtained virtually identical calibration results.

## 5 Results

### 5.1 Computational Benefit

The biggest challenge in the considered analysis is the computational cost of evaluating the likelihood function in the 3-D case, which requires dealing with 61,051-dimensional spatial datasets. To our knowledge, current approaches cannot address this problem with reasonable computational effort (discussed below). The required number of principal components is about 20 for the 3-D case for reasonable accuracy and this means we still need to invert a  $5,000 \times 5,000$  covariance matrix for the likelihood evaluation in the emulation stage for the method due to Higdon et al. (2008). Moreover, the number of parameters to be estimated is 81, and this requires updating more than ten parameter blocks for each iteration of MCMC to obtain a reasonably well-mixed chain. The method of Bhat et al. (2012) requires multiplication of a  $J \times 61,501$  matrix into another  $61,501 \times J$  matrix in the likelihood evaluation with certain number of knots  $J$ , and this makes the likelihood evaluation computationally prohibitive.

The computational time in emulation stage for the 1-dimensional, 2-dimensional and 3-dimensional cases for different methods are illustrated in Figure 1. The computing time shown in the figure is for a system with Intel Xeon E5450 Quad-Core 3.0 GHz and based on the computational complexity for matrix operations involved in each method. We assume that each method has been implemented using

436 Markov chain Monte Carlo maximum likelihood estimation with 25,000 iterations.  
 437 In order to consider the dimensionality of parameter space in our comparison, we  
 438 assume that five parameters are updated as a block in each MCMC run. Our  
 439 method can deal with the 3-D case with a reasonable computational cost. We  
 440 note that while we did not include this in our comparisons, parallel computing  
 441 may further speed up computations for our approach. Since there are 81 param-  
 442 eters in the approach due to Higdon et al. (2008), the method requires updating  
 443 17 parameter blocks for each MCMC iteration in the 3D case.

## 444 **5.2 The Effect of Data Aggregation on Climate Model Cal-** 445 **ibration**

446 In order to study the effect of data aggregation on climate model calibration,  
 447 we conducted a study with pseudo-observational data. The simulated data are  
 448 generated as follows:

- 449 1. Choose the 3-D pattern of UVic ESCM output with  $K_{bg} = 0.2$ ,  $A_{scl} = 1.5$ ,  
 450 and  $C_s = 3.975975$  as the synthetic truth.
- 451 2. Compute three different 3-D patterns of residuals between the observational  
 452 data and the UVic model outputs with  $K_{bg} = 0.1$ ,  $K_{bg} = 0.2$ , and  $K_{bg} = 0.3$ .  
 453 The values for  $A_{scl}$  and  $C_s$  are the same as in Step 1. Average them over  
 454 each location to compute a pseudo-residual. This is a more realistic and  
 455 challenging residual than one obtained by simulation from a simple error  
 456 model, for example a realization from a Gaussian process model. For brevity,  
 457 we describe here just this most challenging case; our methods worked even

458 better in terms of posterior variance when error processes were assumed to  
459 be simpler.

460 3. Superimpose the pseudo residual on the synthetic truth to construct pseudo  
461 observational data in 3-D.

462 4. Aggregate the 3-D pseudo observational data into 2-D and 1-D by integrating  
463 the ocean temperature with respect to water volume.

464 The calibration results based on this simulated example is shown in Figure 2. The  
465 sensitivity test indicates that the posterior distribution of  $K_{bg}$  in the 1-D and the  
466 2-D cases rely on the specification of priors. This deep uncertainty is drastically  
467 reduced when the full data set (3-D) is used. A comparison result based on the real  
468 data from Ocean Atlas 2009 is shown in Figure 3. As in the simulated example, the  
469 calibration results based on the 3-D data are more robust to the prior specification.

470 Using the full pattern of the 3-D data has important benefits as it drastically  
471 reduces the deep uncertainty due to different prior specifications. We hypothesize  
472 that this is because the full non-aggregated spatial patterns contain more infor-  
473 mation about both the observational error and the discrepancy. In order to reflect  
474 the uncertainty due to prior choice to our density estimate for  $K_{bg}$ , we show in  
475 Figure 4 the posterior distributions when the prior is assumed to be with equal  
476 probability any one of the 4 priors considered, along with the resulting AMOC  
477 projections. We define AMOC projection as the annual maximum value of the  
478 meridional overturning streamfunction in the Atlantic between  $0^\circ$  and  $70^\circ\text{N}$ . The  
479 corresponding projections for AMOC change between 1970 to 1999 mean and 2070  
480 to 2099 mean indicate that the unaggregated pattern gives a much narrower 95%  
481 predictive interval than the aggregated ones. Therefore, data aggregation increases



the deep uncertainty surrounding AMOC projection, and using unaggregated data reduces uncertainty regarding the future behavior of the AMOC.

## 6 Discussion

### 6.1 Summary

We propose a computer model calibration approach that is computationally efficient even when dealing with high-dimensional data. By exploiting the orthogonality of a principal components decomposition of the data, this method can keep the computational cost affordable for high-dimensional data with more than 60,000 spatial locations and 250 parameter settings. We apply this method to the problem of calibrating a climate model parameter in an Earth System Model of Intermediate complexity based on observations of the potential temperature. The calibration results show that using 3-D data reduces the uncertainty about  $K_{bg}$  and is more robust to various prior specifications than calibration based on 2-D or 1-D aggregated versions of the data. The results suggest that using unaggregated data is valuable for reducing deep uncertainty associated with different priors. Our simulated examples show that our approach can handle complicated model-observation discrepancies. The method can be easily extended to allow for calibration with multiple tracers – we can simply consider the variance-covariance matrix for all tracers and use its principal components to build an emulator.

## 6.2 Caveats

A general issue with principal components is also worth considering in this context: the principal components for the computer model outputs are selected based on explained variation, and thus there is no guarantee that these leading principal components carry the most important information about the climate parameters. However, our extensive study of the effect of changing the number of principal components suggests that this is not problematic in our context. Our results are consistent with the recent theoretical results in Artemiou and Li (2009) that suggest that there is a low probability that other (non-leading) principal components will have a strong correlation with the climate parameters. We hypothesize that our principal components based approach does not lose valuable information about the climate parameters. In the discrepancy model, one important simplifying assumption is the separability between surface and depth effects. Our simulated example shows that the separability assumption provides a good approximation to the realistic discrepancy process. Non-separable covariance function that combines geodesic distance and Euclidean distance remains as an avenue of ongoing and alive research and subject of future work. Furthermore, our study of calibration with simulated examples shows that even though the number of  $K_{bg}$  settings at which the model is run is relatively sparse, there is enough information to reliably calibrate  $K_{bg}$  based on our emulator.

Our study is also subject to usual caveats with respect to scientific conclusions. First, we ignore the interpolation uncertainty when we compute the density of AMOC projection based on the density of  $K_{bg}$ . Second, the result is based on a single data set, and thus we cannot fully evaluate the effect of structural uncer-

525 tainty due to the model-observation discrepancy and unresolved natural variability  
526 cannot be accounted for; this variability could impact conclusions as well (Olson  
527 et al.). These caveats, of course, apply to almost all existing approaches to climate  
528 model calibration and projection.

## 529 **Acknowledgments**

530 This work was supported by NSF through the Network for Sustainable Climate  
531 Risk Management (SCRiM) under NSF cooperative agreement GEO-1240507.

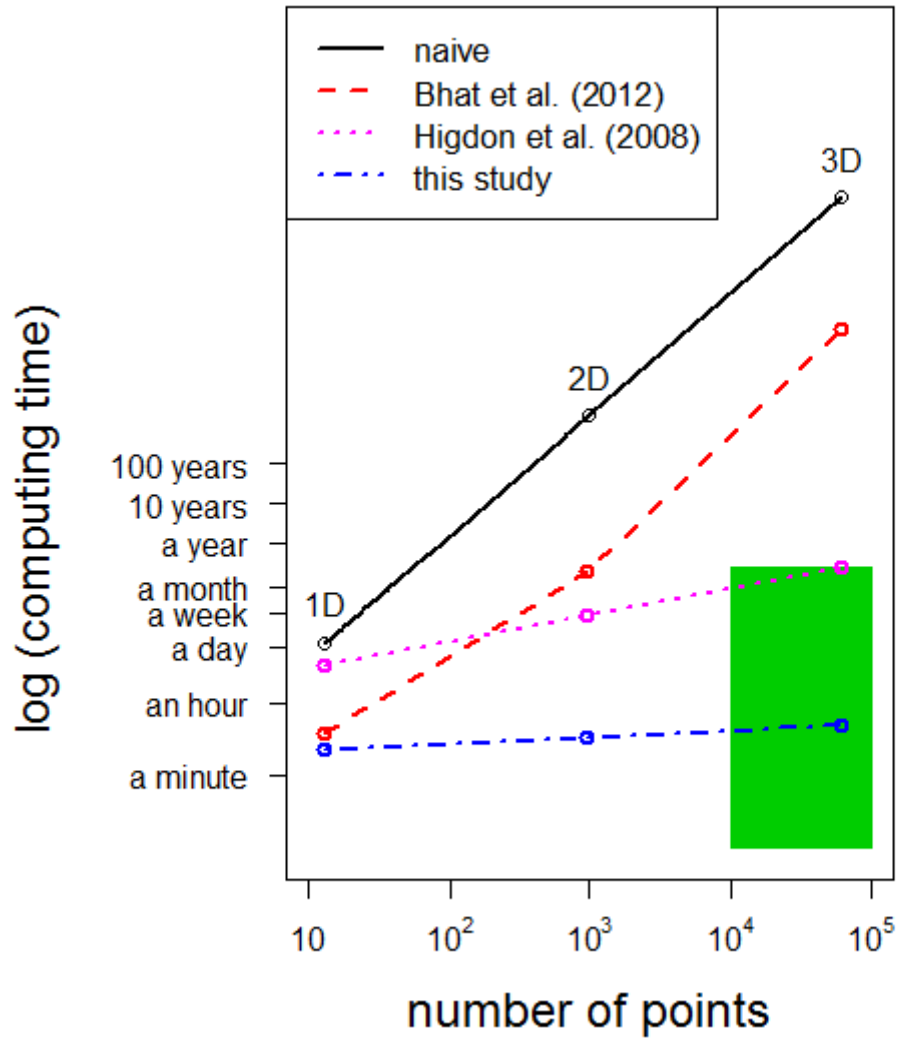


Figure 1: Comparison of computational costs for the emulation step between the current approaches and the new approach. The green box near the bottom right corner shows computing times that are practical, ranging from one second to three months.

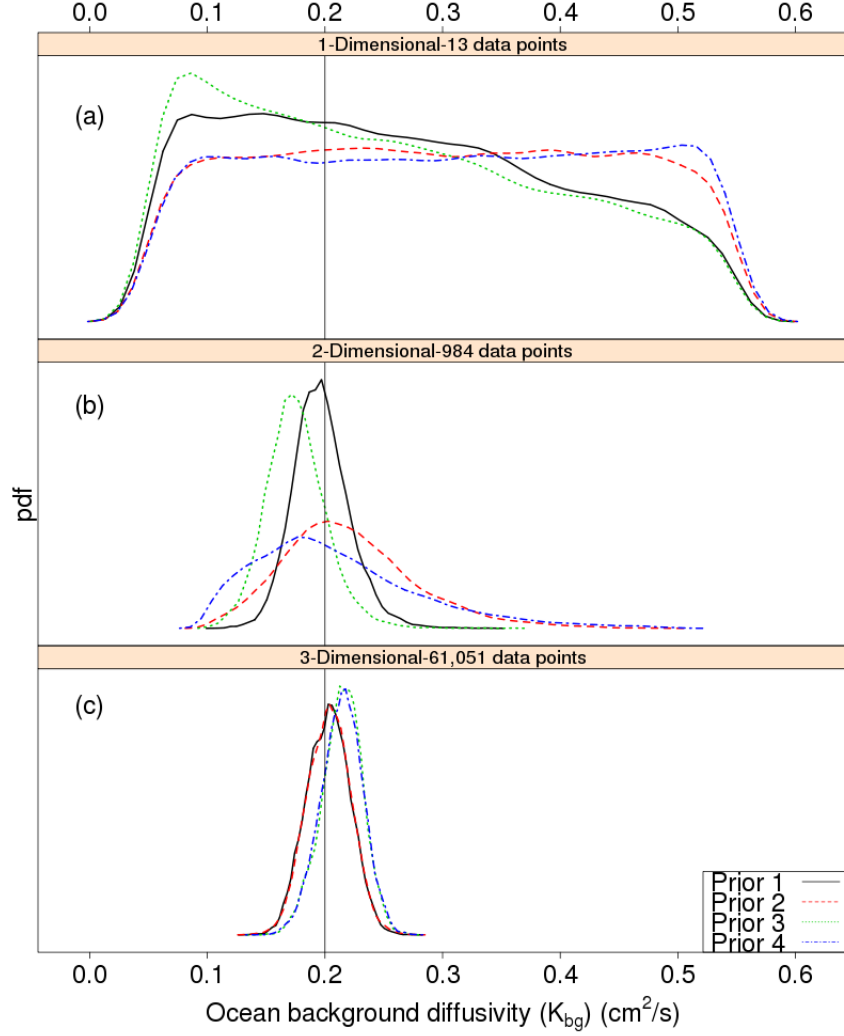


Figure 2: Prior sensitivity test in the simulated example. Calibration of  $K_{bg}$  value based on (a) 1-D depth profile (upper panel), (b) 2-D latitude-depth pattern (middle panel) (c) 3-D non-aggregated data (lower panel). Each line represents posterior density from four different priors:  $(b_v = 2, b_z = 2)$  (Prior 1, solid line),  $(b_v = 2, b_z = 100)$  (Prior 2, dashed line),  $(b_v = 100, b_z = 2)$  (Prior 3, dotted line), and  $(b_v = 100, b_z = 100)$  (Prior 4, dot-dashed line). The solid vertical line represents the true value of  $K_{bg}$  in the synthetic truth.

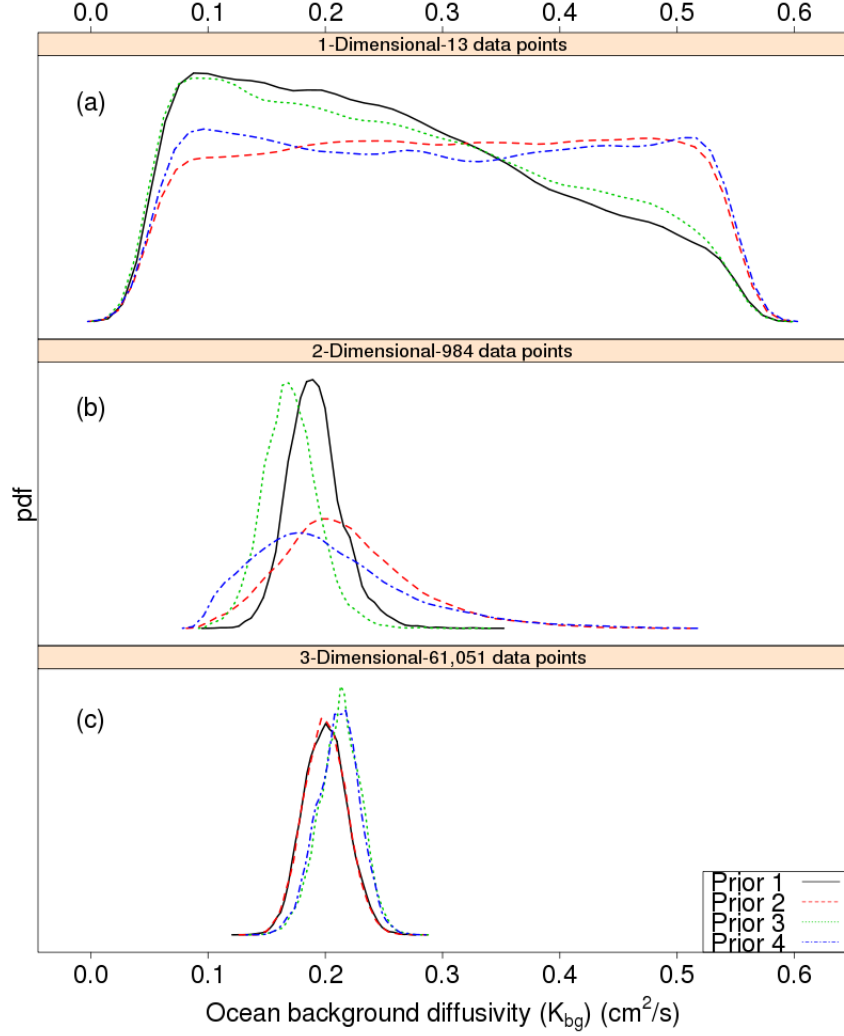


Figure 3: Prior sensitivity test using observational data from the World Ocean Atlas 2009. Calibration results based on (a) 1-D depth profile (upper panel), (b) 2-D latitude-depth pattern (middle panel) (c) 3-D non-aggregated data (lower panel). Each line represents posterior density from four different priors: ( $b_v = 2, b_z = 2$ ) (Prior 1, solid line), ( $b_v = 2, b_z = 100$ ) (Prior 2, dashed line), ( $b_v = 100, b_z = 2$ ) (Prior 3, dotted line), and ( $b_v = 100, b_z = 100$ ) (Prior 4, dot-dashed line).

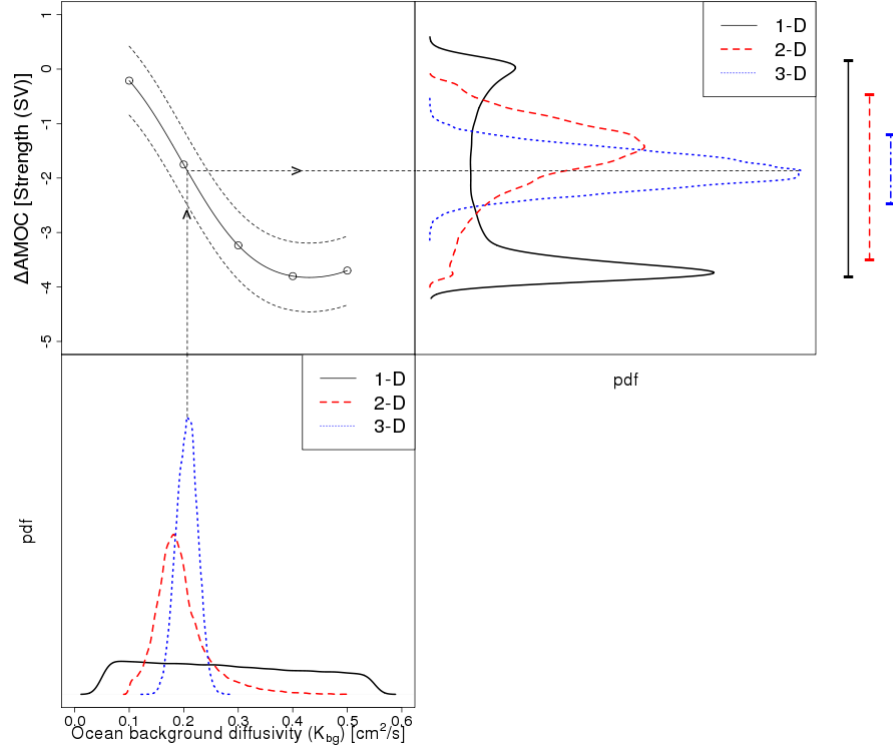


Figure 4: Combined posterior densities of  $K_{bg}$  from different prior specifications (lower left), the relationship between  $K_{bg}$  and projected AMOC change of the 2070 - 2099 mean from the 1970 - 1999 mean (upper left), and the resulting AMOC change projections (upper right) using 1-D (solid line), 2-D (dashed line) and 3-D (dotted line) data with their 95% credible intervals (bars at the right)

## References

- R. Alley, T. Berntsen, N. L. Bindoff, Z. Chen, A. Chidthaisong, P. Friedlingstein, J. Gregory, G. Hegerl, M. Heimann, B. Hewitson, F. Joos, J. Jouzel, V. Kattsov, U. Lohmann, M. Manning, T. Matsuno, M. Molina, N. Nicholls, J. Overpeck, D. Qin, G. Raga, V. Ramaswamy, J. Ren, M. Rusticucci, S. Solomon, R. Somerville, T.F Stocker, P. Stott, P. Whetton, R.A. Wood, and D. Wratt. *Climate Change 2007: The Physical Science Basis: Summary for Policymakers: Contribution of Working Group I to the Fourth Assessment Report of the Intergovernmental Panel on Climate Change*, 2007. IPCC.
- J.I. Antonov, D. Seidov, T.P. Boyer, R.A. Locarnini, A.V. Mishonov, H.E. Garcia, O.K. Baranova, M.M. Zweng, and D.R. Johnson. *World Ocean Atlas 2009, Volume 2: Salinity*, S. Levitus, Ed., NOAA Atlas NESDIS 69, US Government Printing Office, Washington, DC. page 184, 2010.
- A. Artemiou and B. Li. On principal components and regression: A statistical explanation of a natural phenomenon. *Statistica Sinica*, 19(4):1557–1565, 2009.
- M.J. Bayarri, J.O. Berger, J. Cafeo, G. Garcia-Donato, F. Liu, J. Palomo, R.J. Parthasarathy, R. Paulo, J. Sacks, and D. Walsh. Computer model validation with functional output. *The Annals of Statistics*, 35(5):1874–1906, 2007.
- K.S. Bhat, M. Haran, and M. Goes. Computer model calibration with multivariate spatial output: A case study. *Frontiers of Statistical Decision Making and Bayesian Analysis*, pages 168–184, 2010.
- K.S. Bhat, M. Haran, R. Olson, and K. Keller. Inferring likelihoods and climate



- 554 system characteristics from climate models and multiple tracers. *Environmetrics*,  
555 23(4):345–362, 2012.
- 556 F. Bryan. Parameter sensitivity of primitive equation ocean general circulation  
557 models. *Journal of Physical Oceanography*, 17(7):970–985, 1987.
- 558 H. L. Bryden. New polynomials for thermal expansion, adiabatic temperature gra-  
559 dient and potential temperature of sea water. *Deep Sea Research and Oceano-*  
560 *graphic Abstracts*, 20(4):401–408, 1973.
- 561 N. Cressie. Models for spatial processes. *Statistical Methods for Physical Science*,  
562 28(C):93–124, 1994.
- 563 D. Drignei, C.E. Forest, and D. Nychka. Parameter estimation for computationally  
564 intensive nonlinear regression with an application to climate modeling. *The*  
565 *Annals of Applied Statistics*, 2(4):1217–1230, 2008.
- 566 N.P. Fofonoff. Computation of potential temperature of seawater for an arbitrary  
567 reference pressure. *Deep Sea Research*, 24(5):489–491, 1977.
- 568 C.E. Forest, P.H. Stone, and A.P. Sokolov. Constraining climate model parameters  
569 from observed 20th century changes. *Tellus A*, 60(5):911–920, 2008.
- 570 A. Gnanadesikan. A simple predictive model for the structure of the oceanic  
571 pycnocline. *Science*, 283(5410):2077–2079, 1999.
- 572 T. Gneiting. Strictly and non-strictly positive definite functions on spheres. *arXiv*  
573 *preprint arXiv:1111.7077*, 2011.

574 M. Goes, N.M. Urban, R. Tonkonojenkov, M. Haran, A. Schmittner, and K. Keller.  
575 What is the skill of ocean tracers in reducing uncertainties about ocean diapyc-  
576 nal mixing and projections of the Atlantic Meridional Overturning Circulation?  
577 *Journal of Geophysical Research: Oceans*, 115(C12006), 2010.

578 T. Hastie, R. Tibshirani, and J. Friedman. *The elements of statistical learning:*  
579 *data mining, inference, and prediction*. Springer, 2009.

580 D. Higdon. A process-convolution approach to modelling temperatures in the  
581 North Atlantic Ocean. *Environmental and Ecological Statistics*, 5(2):173–190,  
582 1998.

583 D. Higdon. Space and space-time modeling using process convolutions. *Quantita-*  
584 *tive methods for current environmental issues*, 2002.

585 D. Higdon, J. Gattiker, B. Williams, and M. Rightley. Computer model calibration  
586 using high-dimensional output. *Journal of the American Statistical Association*,  
587 103(482):570–583, 2008.

588 K.L. Jordan. Discrete representations of random signals. *technical report*, 1961.  
589 Massachusetts Institute of Technology Technical Report 378.

590 Klaus Keller, Matt Hall, Seung-Rae Kim, David F Bradford, and M Oppenheimer.  
591 Avoiding dangerous anthropogenic interference with the climate system. *Cli-*  
592 *matic Change*, 73(3):227–238, 2005.

593 Klaus Keller, Curtis Deutsch, Matthew G Hall, and David F Bradford. Early  
594 detection of changes in the north atlantic meridional overturning circulation:

- 595 implications for the design of ocean observation systems. *Journal of Climate*,  
596 20(2):145–157, 2007.
- 597 M.C. Kennedy and A. O’Hagan. Bayesian calibration of computer models. *Journal*  
598 *of the Royal Statistical Society. Series B (Statistical Methodology)*, 63(3):425–  
599 464, 2001.
- 600 R.M. Key, A. Kozyr, CL Sabine, K. Lee, R. Wanninkhof, JL Bullister, RA Feely,  
601 FJ Millero, C. Mordy, and T.H. Peng. A global ocean carbon climatology:  
602 Results from Global Data Analysis Project (GLODAP). *Global Biogeochemical*  
603 *Cycles*, 18(GB4031), 2004.
- 604 F. Liu, MJ Bayarri, and JO Berger. Modularization in bayesian analysis, with  
605 emphasis on analysis of computer models. *Bayesian Analysis*, 4(1):119–150,  
606 2009.
- 607 RA Locarnini, AV Mishonov, JI Antonov, TP Boyer, HE Garcia, OK Baranova,  
608 MM Zweng, and DR Johnson. *World Ocean Atlas 2009, Volume 1: Tempera-*  
609 *ture*, S. Levitus, Ed., NOAA Atlas NESDIS 68, US Government Printing Office,  
610 Washington, DC. page 184, 2010.
- 611 J. R. Lovett. Merged seawater sound-speed equations. *The Journal of the Acous-*  
612 *tical Society of America*, 63:1713–1718, 1978.
- 613 R. Olson, R. Sriver, M. Haran, W. Chang, N.M. Urban, and K. Keller. What is the  
614 effect of unresolved internal climate variability on climate sensitivity estimates?  
615 *Journal of Geophysical Research: Atmospheres*. under revision.
- 616 R. Olson, R. Sriver, M. Goes, N.M. Urban, H.D. Matthews, M. Haran, and

- 617 K. Keller. A climate sensitivity estimate using Bayesian fusion of instrumen-  
618 tal observations and an Earth System model. *Journal of Geophysical Research:*  
619 *Atmospheres*, 117(D04103), 2012.
- 620 J. Rougier. Comment on article by Sanso et al. *Bayesian Analysis*, 3(1):45–56,  
621 2008.
- 622 J. Sacks, W.J. Welch, T.J. Mitchell, and H.P. Wynn. Design and analysis of  
623 computer experiments. *Statistical Science*, 4(4):409–423, 1989.
- 624 B. Sanso and C.E. Forest. Uncertainty quantification: Statistical calibration of  
625 climate system properties. *Applied Statistics*, 58(4):485–03, 2009.
- 626 A. Schmittner, N.M. Urban, K. Keller, and D. Matthews. Using tracer observations  
627 to reduce the uncertainty of ocean diapycnal mixing and climate–carbon cycle  
628 projections. *Global Biogeochemical Cycles*, 23(4), 2009.
- 629 L. Sriviver, M. Nathan, R. , we, and K. Keller. Toward a physically plausible upper  
630 bound of sea-level rise projections. *Climate Change*, 115(3–4):893–902.
- 631 UNESCO. Tenth report of the joint panel on oceanographic tables and standards.  
632 *Technical report*, 1981. UNESCO Technical Reports on Marine Science 36.
- 633 A.J. Weaver, M. Eby, E.C. Wiebe, C.M. Bitz, P.B. Duffy, T.L. Ewen, A.F. Fan-  
634 ning, M.M. Holland, A. MacFadyen, and H.D. Matthews. The UVic Earth Sys-  
635 tem Climate Model: Model description, climatology, and applications to past,  
636 present and future climates. *Atmosphere-Ocean*, 39(4):361–428, 2001.
- 637 C. Wunsch and R. Ferrari. Vertical mixing, energy, and the general circulation of  
638 the oceans. *Annual Review of Fluid Mechanics*, 36:281–314, 2004.

639 Z. Zhu and Y. Wu. Estimation and prediction of a class of convolution-based  
640 spatial nonstationary models for large spatial data. *Journal of Computational*  
641 *and Graphical Statistics*, 19(1):74–95, 2010.